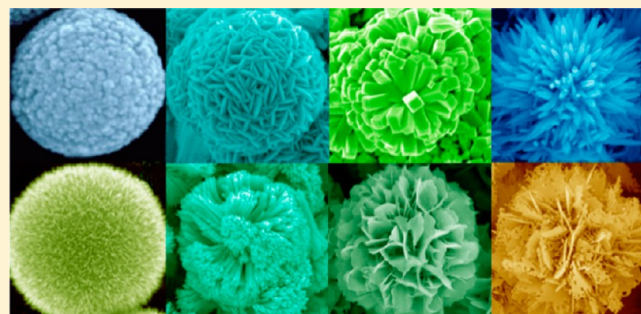


# Hierarchical SnO<sub>2</sub> Nanostructures: Recent Advances in Design, Synthesis, and Applications

Hongkang Wang and Andrey L. Rogach\*

Department of Physics and Materials Science & Centre for Functional Photonics (CFP), City University of Hong Kong, Hong Kong SAR

**ABSTRACT:** Complex three-dimensional hierarchical structures assembled from well-defined low-dimensional nanosized building blocks are an interesting class of nanomaterials with a rich variety of tunable physicochemical properties. Tin dioxide (SnO<sub>2</sub>) is an important *n*-type wide-bandgap semiconductor with wide applications in transparent conductive films, gas sensors, lithium-ion batteries, and solar cells. In this review, we outline synthetic strategies of hierarchical SnO<sub>2</sub> nanostructures in terms of the dimension and the facet control of their constituting building blocks, creation of porous and hollow structures, as well as their modification by doping and loading with other elements. The design of hierarchical SnO<sub>2</sub> nanostructures with an improved performance in lithium-ion



batteries, sensitized solar cells, and gas-sensing applications is reviewed.

**KEYWORDS:** hierarchical structures, SnO<sub>2</sub> nanostructures, morphology engineering, doping, facet control, gas sensing, lithium-ion batteries, solar cells

## 1. INTRODUCTION

Synthesis of wide-bandgap oxide nanomaterials with controllable shapes and sizes has been an active area of research over the last two decades, because of their shape- and size-dependent physical, chemical, electronic, optical, and catalytic properties.<sup>1–7</sup> In particular, tin dioxide (SnO<sub>2</sub>) nanomaterials have attracted considerable attention, because of their wide applications in lithium-ion batteries,<sup>8–17</sup> gas sensors,<sup>18–26</sup> sensitized solar cells,<sup>27–33</sup> and catalysts.<sup>34–37</sup> Different morphologies of low-dimensional SnO<sub>2</sub> nanostructures have been reported, such as zero-dimensional (0D) nanoparticles;<sup>1,7</sup> one-dimensional (1D) nanorods,<sup>38</sup> nanobelts,<sup>6</sup> nanowires<sup>22</sup> and nanotubes;<sup>39</sup> and two-dimensional (2D) nanosheets.<sup>2</sup> Three-dimensional (3D) hierarchical architectures self-assembled from these low-dimensional nanostructured building blocks via interactions such as van der Waals forces, as well as hydrogen, ionic, and covalent bonding, are an interesting class of nanomaterials.<sup>40–45</sup> Besides, the doping of SnO<sub>2</sub>-based nanomaterials offers a convenient way to tailor their electrical, optical, and microstructural properties.<sup>19,34,35,46–51</sup> In this respect, development of suitable synthetic strategies is crucial to provide the desired property control. Related to SnO<sub>2</sub>, the hydrothermal synthesis has been most widely used, because of its convenient manipulation combined with flexible control over the size and morphology of the resulting (nano)-structures.<sup>52</sup> It runs under high temperature and pressure, which change the solubility of reactants and facilitate specific chemical reactions. In this review, solution-based synthetic routes toward hierarchical SnO<sub>2</sub> nanostructures are reviewed,

which are most commonly conducted within the general two paths: direct hydrothermal synthesis or template synthesis, using hierarchical precursors as conformal templates. We outline the design principles and the synthetic strategies of hierarchical SnO<sub>2</sub> nanostructures, such as control of their unit's dimensionality and the related facet engineering of 2D building blocks; fabrication of highly porous structures and the structures with hollow interior; and doping. Design of hierarchical nanostructures refers to specific ways of assembly of their constituting building blocks in a desired and controlled manner, resulting in a variety of architectures. We finally outline the most important applications of hierarchical SnO<sub>2</sub> nanostructures in lithium-ion batteries, gas sensors, and solar cells. By focusing on the hierarchical SnO<sub>2</sub> nanostructures, we hope to provide better understanding on their design principles and useful physicochemical properties when used in energy storage, gas sensing and energy conversion, uncovering new possibilities and advancing future research.

## 2. DESIGN AND SYNTHETIC STRATEGIES OF HIERARCHICAL SnO<sub>2</sub> NANOSTRUCTURES

### 2.1. Dimensionality Control of Building Units.

The dimensionality of building blocks of hierarchical SnO<sub>2</sub>

**Special Issue:** Celebrating Twenty-Five Years of Chemistry of Materials

**Received:** June 5, 2013

**Revised:** August 5, 2013

nanostructures can be chosen on purpose from a variety of 0D, 1D, and 2D units, providing specific morphologies of the resulting products whose particular properties are thus adjusted on demand. In mesoporous SnO<sub>2</sub> spheres composed of 0D units,<sup>13,14,53</sup> the constituting nanoparticles are often randomly attached without a specific orientation, resulting in numerous grain boundaries, even though such structures typically exhibit large specific surface areas desired for applications such as gas sensing.<sup>7,22</sup> However, the grain boundaries act as electron capturers, hindering efficient electron transport.<sup>54</sup> In contrast, hierarchical nanostructures assembled from single-crystalline 1D building blocks such as SnO<sub>2</sub> nanorods, nanowires, or nanotubes provide direct electrical pathways for photo-generated electrons, which typically results in greatly improved electron transport rates,<sup>46,55,56</sup> so that they can be utilized in photovoltaic devices. 2D nanosheets/nanoplates with a large percentage of specific (often high-index) exposed surface facets are crucial for application areas such as catalysis and electrocatalysis,<sup>1,57–59</sup> as well as for lithium-ion batteries. The energy barriers for Li<sup>+</sup> insertion into the (001) and (101) facets of anatase TiO<sub>2</sub> crystals have been theoretically estimated as 1.33 and 2.73 eV, respectively, suggesting much easier insertion/extraction of Li<sup>+</sup> ions through the high-energy (001) facets, compared to the most stable (101) surfaces.<sup>15,60</sup> Electrochemical studies confirmed the enhanced lithium insertion activity of (001) facets, ascribed to the synergistic contribution of a faster interfacial charge transfer and a more open pathway along the *c*-axis.<sup>61</sup>

The dimensionality of constituting SnO<sub>2</sub> building blocks synthesized by solution-based chemical routes, which typically involve the hydrolysis of tin precursors and the following crystallization of tin dioxide (SnO<sub>2</sub>) nuclei, most often under hydrothermal conditions, depends on a variety of parameters, such as the type and concentration of tin precursor, the pH value of the aqueous solution, as well as the possible additives and co-solvents employed (see Table 1).

0D SnO<sub>2</sub> building blocks are generally obtained via hydrothermal methods, using tin salts such as SnCl<sub>4</sub>, SnCl<sub>2</sub>, or K<sub>2</sub>SnO<sub>3</sub> in the aqueous solutions containing water-soluble carbohydrates (e.g., glucose, furfural), without the presence of any other additives.<sup>14,62,63</sup> Because of the hydrothermal carbonization, hydrophilic carbon spheres are produced through the dehydration, polymerization, and carbonization of carbohydrates in the hydrothermal process.<sup>13</sup> The carbonaceous materials serve as removable templates in the follow-up calcination, and can be used to prepare mesoporous, hollow, and/or core-shell SnO<sub>2</sub> microspheres aggregated from 0D nanoparticles by hydrothermal treatment of (i) the mixture of tin precursor and carbohydrate, (ii) the tin precursor and hydrothermally carbonized carbohydrate, or (iii) the mixture of SnO<sub>2</sub> nanoparticle sols and carbohydrates.

1D SnO<sub>2</sub> building blocks are generally obtained via hydrothermal methods using Sn(IV) salts such as SnCl<sub>4</sub> or Na<sub>2</sub>SnO<sub>3</sub> in alkaline solutions typically adjusted to the desired pH by NaOH, and their formation is affected by the NaOH:Sn(IV) molar ratio. Sn(II) salts such as SnCl<sub>2</sub> or SnSO<sub>4</sub> can also be used to prepare 1D SnO<sub>2</sub> nanorods in the presence of oxidizing agents such as H<sub>2</sub>O<sub>2</sub>, or in acidic solutions containing H<sub>2</sub>SO<sub>4</sub>, which can oxidize Sn(II) into Sn(IV).<sup>68,69</sup>

In the case of the most common use of a water-soluble Sn(IV) precursor such as SnCl<sub>4</sub> undergoing hydrolysis in basic aqueous solution:

**Table 1. Representative Examples of the Unit Dimensions of SnO<sub>2</sub> Building Blocks Achieved in Solution-Based Synthetic Approaches**

unit dimension	tin precursor	additive(s) <sup>a</sup>	solvent(s)/co-solvent(s)	ref
0D particle	SnCl <sub>4</sub>	D-glucose	H <sub>2</sub> O/ethanol	14
0D particle	SnCl <sub>2</sub>	D-glucose	H <sub>2</sub> O	62
0D particle	K <sub>2</sub> SnO <sub>3</sub>	glucose	H <sub>2</sub> O	63
0D particle	K <sub>2</sub> SnO <sub>3</sub>	urea, thiourea, ethyldiamine	H <sub>2</sub> O/ethanol	64
1D rod	Na <sub>2</sub> SnO <sub>3</sub>	NaOH	H <sub>2</sub> O	65
1D rod	SnCl <sub>4</sub>	CTAB, HMT	basic H <sub>2</sub> O/ethanol	66
1D cone	SnCl <sub>4</sub>	PAA, NaOH	H <sub>2</sub> O	67
1D rod	SnCl <sub>4</sub>	SDS, NaOH	heptane/hexanol	38
1D rod	SnCl <sub>2</sub>	NaOH, H <sub>2</sub> O <sub>2</sub>	H <sub>2</sub> O	68
1D prickle	SnSO <sub>4</sub>	H <sub>2</sub> SO <sub>4</sub>	H <sub>2</sub> O	69
2D sheet	SnCl <sub>2</sub>	sodium citrate, NaOH	H <sub>2</sub> O	70, 71
2D sheet	SnCl <sub>2</sub>	urea, NaOH	H <sub>2</sub> O/ethanol	41
2D sheet	SnSO <sub>4</sub>	sodium citrate	basic H <sub>2</sub> O/alcohol	72
2D sheet	SnSO <sub>4</sub>	none	H <sub>2</sub> O	73
2D sheet	SnCl <sub>2</sub>	H <sub>2</sub> C <sub>2</sub> O <sub>4</sub> , HCl, N <sub>2</sub> H <sub>4</sub>	H <sub>2</sub> O	74
2D sheet	SnCl <sub>2</sub>	none	basic H <sub>2</sub> O/ethanol	2
2D sheet	SnCl <sub>2</sub>	NaF	H <sub>2</sub> O	75

<sup>a</sup>CTAB = cetyltrimethylammonium bromide; HMT = hexamethylenetetramine; PAA = poly(acrylic acid); SDS = sodium dodecyl sulfate.

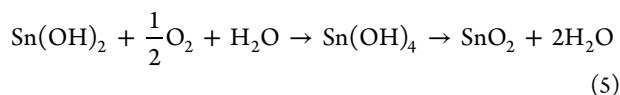
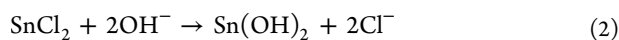


higher Sn<sup>4+</sup> ion concentration and higher pH accelerate the nucleation process, which results both in a higher nuclei concentration and in higher growth rates of nanoparticles. Cheng et al.<sup>76</sup> reported the synthesis of single-crystalline SnO<sub>2</sub> nanorods with relatively small size (15–20 nm in length and 2.5–5 nm in diameter) by hydrothermal treatment of SnCl<sub>4</sub> in a basic mixture of water and alcohol (pH ~12). Using nonaqueous solvents, Zhang et al.<sup>38</sup> prepared dendritic SnO<sub>2</sub> nanorods ~10 nm × 200 nm in size via hydrothermal treatment of the precursor solution containing SnCl<sub>4</sub>, NaOH, sodium dodecyl sulfate (SDS) in heptane and hexanol at 200 °C, and emphasized that the appropriate molar ratio of OH<sup>-</sup> to Sn(IV) is ~20–30 for the growth of SnO<sub>2</sub> nanorods, whose formation was attributed to an aggregation mechanism via oriented attachment rather than the classical Ostwald ripening. Irregular SnO<sub>2</sub> nuclei are formed at the initial stage, which then rearrange to minimize the total surface energy, resulting in the formation of relatively large nanorods.

Birkel et al.<sup>77</sup> have shown that the morphology of anisotropic SnO<sub>2</sub> nanorods obtained by polycondensation of hydrated tin tetrachloride (SnCl<sub>4</sub>·5H<sub>2</sub>O) at basic pH (pH 11–14) strongly depends on the cations of the precursor base (LiOH, NaOH, KOH, RbOH<sub>3</sub>, CsOH<sub>3</sub>, tetramethylammonium hydroxide and NH<sub>4</sub>OH). The surface energies of SnO<sub>2</sub> facets follow the trend (110) < (100) < (101) < (001), assuming the preferential growth direction along the *c*-axis. The enclosing faces of a crystal are usually those with the lowest growth rate (i.e., the lowest surface energy), while the surface energy is strongly affected by foreign ions adsorbed to the crystal faces. Molecular dynamics simulations showed that the adsorption energy of cations on the (110) crystal faces changes as Na<sup>+</sup> > K<sup>+</sup> > Rb<sup>+</sup> > Cs<sup>+</sup> > tetramethylammonium (TMA<sup>+</sup>) > ammonium (NH<sub>4</sub><sup>+</sup>),

rendering NaOH the most favorable additive for the growth of 1D SnO<sub>2</sub> nanostructures, with [001] direction as the growth axis and (110) as the family of enclosing facets.<sup>38,76,77</sup>

2D SnO<sub>2</sub> nanostructures can be generally obtained by hydrothermally treating the precursor solution containing Sn(II) salts in the alkaline aqueous solution, sometimes mixed with ethanol. The oxidation of Sn(II) into Sn(IV), the oxidation into Sn(IV) is necessary for the synthesis of SnO<sub>2</sub>, which can be performed not only by adding oxidizing agents mentioned above, but also by dissolving oxygen in the precursor solution. Wu et al.<sup>41</sup> prepared 3D hierarchical SnO<sub>2</sub> nanostructures composed of 2D nanosheets, using SnCl<sub>2</sub> as tin source and NaOH and urea as controlling agents, suggesting that the oxidation process is crucial for the formation of the nanosheet structure, while the byproduct of SnO would be produced because of the limited dissolved oxygen. Chemical reactions for the formation of hierarchical SnO<sub>2</sub> nanosheets include both the hydrolysis and oxidation of Sn(II) ions in a basic aqueous solution:



Different from the case of Sn(IV) precursor (reaction 1), an intermediate product of Sn(OH)<sub>2</sub> is initially formed in the alkaline aqueous solution of Sn(II) salts, which further undergoes dehydration and oxidation to form SnO<sub>2</sub>, according to reactions 3–5. The romarchite SnO adopts a tetragonal layered structure with an AA... stacking sequence of slabs, where each slab consists of a square planar arrangement of oxygen ions sandwiched between sublayers of Sn ions.<sup>78</sup> The layered structure of the intermediate Sn(OH)<sub>2</sub> or SnO may be the reason for the preferential formation of 2D nanostructures by using Sn(II) salts as the tin source.

The morphology and dimensionality of SnO<sub>2</sub> building blocks can also be influenced by solvents. Guo et al.<sup>79</sup> demonstrated that flowerlike nanostructures consisted of interleaving nanosheets and hollow microspheres composed of 0D nanoparticles can be obtained in the SnCl<sub>2</sub>–NaOH system by using a mixture of water and ethanol as the solvent, respectively. Lou et al.<sup>64</sup> pointed out that the polarity of such a mixed solvent has a significant influence on the final morphology of the SnO<sub>2</sub> products.

Introduction of additives is yet another useful strategy to control the dimensionality of SnO<sub>2</sub> building units. The additives are able to preferentially adsorb on certain crystal facets and change their relative stability in terms of the surface energy, tune the growth rates, and thus tailor the shape and the dimensionality of the growing crystals.<sup>80</sup> Especially, organic long-chain surfactants such as poly(acrylic acid) (PAA),<sup>64</sup> poly(ethylene glycol) (PEG),<sup>48,79</sup> and cetyltrimethylammonium bromide (CTAB),<sup>48</sup> play an important role in the formation of 1D SnO<sub>2</sub> nanostructures and their hierarchical assembly. These flexible nonionic polymers containing numerous hydrophilic and hydrophobic sites direct the aggregation of SnO<sub>2</sub> nuclei and the following growth of 1D SnO<sub>2</sub> crystals.

Facet engineering of nanocrystalline metal oxides is an important strategy to explore and realize their physicochemical properties. This is because the surface atomic structures, such as atom steps, ledges, kinks, and dangling bonds largely determine their chemical reactivity and selectivity, which is extremely important for several areas of potential applications, such as heterogeneous catalysis, gas sensing, and energy conversion and storage.<sup>1,4,80–84</sup> 2D metal oxide nanosheets with a large percentage of certain facets exposed, and thus highly reactive surfaces have been widely explored.<sup>5,85–87</sup> However, surfaces with high reactivity usually diminish rapidly during the crystal growth to minimize the total surface energy.<sup>4</sup> Considerable efforts have been thus devoted to their kinetic and thermodynamic control, in particular by using fluorine adsorbate atoms<sup>4,80</sup> able to attach to specific facets of metal oxides and prevent their growth along that particular direction. This approach has been applied for the synthesis of anatase TiO<sub>2</sub> single crystals with a high percentage of reactive {001} facets exposed through surface fluorine passivation using hydrofluoric acid.<sup>4,83,87–89</sup> Han et al.<sup>1</sup> reported octahedron-shaped SnO<sub>2</sub> nanoparticles with exposed high-index {221} facets by exploiting the coordinative/adsorption effect of HCl and poly(vinyl pyrrolidone) (PVP). Recently, relative stability of the most common exposed facets of 2D SnO<sub>2</sub> nanosheets passivated by NaF has been addressed.<sup>75</sup> The passivation effect of fluorine adsorbate atoms has been estimated by the first-principle calculations<sup>90,91</sup> of the surface free energy  $\gamma$  for clean and F-terminated SnO<sub>2</sub> (001), (110), (10 $\bar{2}$ ), and (11 $\bar{3}$ ) crystal facets, respectively. As shown in Table 2, the (110) surface is

**Table 2. Calculated Surface Free Energy ( $\gamma$ ) for Four Different SnO<sub>2</sub> Crystal Facets, Clean and Terminated by F Atoms Using Two Sets of Specified Pseudo-potential Configurations<sup>a</sup>**

surface	Surface Free Energy, $\gamma$ [J/m <sup>2</sup> ]			
	Sn{5s <sup>2</sup> 4d <sup>10</sup> 5p <sup>2</sup> }, O{2s <sup>2</sup> 2p <sup>5</sup> }, F{2s <sup>2</sup> 2p <sup>5</sup> }		Sn{5s <sup>2</sup> 5p <sup>2</sup> }, O{2s <sup>2</sup> 2p <sup>5</sup> }, F{2s <sup>2</sup> 2p <sup>5</sup> }	
	clean	F-terminated	clean	F-terminated
001	1.62	0.54	1.68	0.57
110	0.91	0.13	0.92	0.12
10 $\bar{2}$	1.5	−0.15	1.55	−0.138
11 $\bar{3}$	2.02	0.076	2.07	0.099

<sup>a</sup>Reproduced with permission from ref 75.

the most stable one among four clean surfaces, while fluorination significantly lowers their energy ( $\gamma$ ), because of the high Sn–F bonding energy, making (10 $\bar{2}$ ) and (11 $\bar{3}$ ) surfaces the most stable ones. Among these two, the (10 $\bar{2}$ ) surface is more stable than the (11 $\bar{3}$ ) surface, which supported experimental findings related to formation mechanism of exposed {11 $\bar{3}$ } and {10 $\bar{2}$ } facets (see Figure 1) under different fluorine concentrations.<sup>75</sup>

**2.2. Porous Hierarchical SnO<sub>2</sub> Nanostructures.** Herein, porous hierarchical nanostructures are defined as architectures constructed from nanosized building blocks that possess interconnected pores on a variety of size scales, termed in ref 42 as micropores (<2 nm), mesopores (2–50 nm), and macropores (>50 nm). Such porous structures provide very large active surface areas, favoring the diffusion of guest molecules. The most common approach to create those structures for SnO<sub>2</sub> is to induce the formation of pores by thermal treatment, such as thermal decomposition,<sup>15</sup> thermal

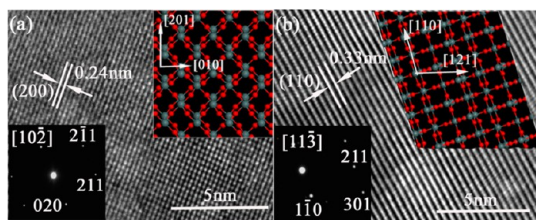


**Figure 1.** High-resolution transmission electron microscopy (HRTEM) images of (a)  $\{10\bar{2}\}$  faceted and (b)  $\{11\bar{3}\}$  faceted  $\text{SnO}_2$  nanosheets with insets showing corresponding electron diffraction patterns and the schematic illustration of  $\{10\bar{2}\}$  and  $\{11\bar{3}\}$  atomic planes, respectively. (Reproduced with permission from ref 75. Copyright 2013, Wiley–VCH, Weinheim, Germany.)

melting–recrystallization,<sup>22</sup> and thermal oxidation.<sup>78</sup> Jiang et al.<sup>15</sup> reported hierarchical  $\text{SnO}_2$  nanostructures consisting of porous nanorods as building blocks (Figure 2), which were

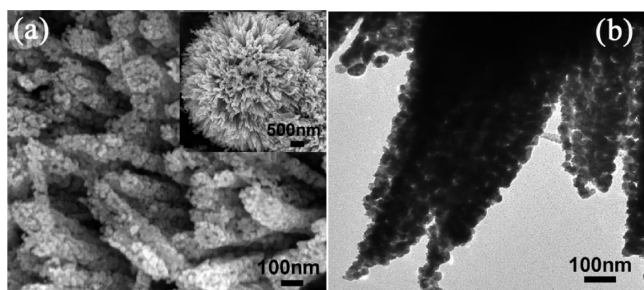


**Figure 2.** (a) Scanning electron microscopy (SEM) images and (b) transmission electron microscopy (TEM) images of hierarchical  $\text{SnO}_2$  nanostructures consisting of porous nanorods as building blocks. The inset in panel (a) presents a full view of a single flower-like structure. (Reproduced with permission from ref 92. Copyright 2011, Royal Society of Chemistry, London.)

obtained from the  $\text{SnC}_2\text{O}_4$  nanorods transformed into a highly porous structure consisting of interconnected nanoparticles after the thermal decomposition and removal of their organic component during the calcination at 500 °C in air. In a similar way, Sun et al.<sup>72</sup> prepared porous  $\text{SnO}_2$  hierarchical 2D nanosheets by thermal annealing the precursor precipitates, which were synthesized by hydrothermally treating the  $\text{SnSO}_4\text{--Na}_3\text{C}_6\text{H}_5\text{O}_7$  in basic water/alcohol solution. The formation of

the porous nanosheets was attributed to the thermal decomposition of the organic component (citrate salt) and the release of gas in confined space during the sintered process. In both cases, the organic additives were employed to achieve the formation of pores.

In another approach, we reported the formation of porous hierarchical  $\text{SnO}_2$  nanostructures consisting of layer-by-layer assembled 2D nanosheets via the thermal oxidation of the  $\text{SnO}$  precursor.<sup>78</sup>  $\text{SnO}$  nanosheets also served as conformal sacrificial templates for the fabrication of layered  $\text{SnO}/\text{SnO}_2$  nanostructures, through the calcination in air. Since  $\text{SnO}$  is soluble in strong acids, the inner  $\text{SnO}$  part of such a composite can be conveniently removed via dissolution in  $\text{HCl}$ , leaving behind partially disassembled  $\text{SnO}_2$  nanosheets with porous structures.

**2.3. Hierarchical  $\text{SnO}_2$  Nanostructures with a Hollow Interior.** Hierarchical nanostructures with hollow interior provide an extraordinarily high surface area, robust stability, and low material density, rendering them lightweight materials with promising applications for nanoreactors, drug delivery, catalysis, energy storage, and gas sensing.<sup>3,16,73,92,93</sup> The general approach for the fabrication of hollow structures involves growth of desired materials on the hard templates such as polymer, silica, and carbon, which can be removed by chemical etching or thermal decomposition, or soft templates such as emulsion micelles and even bubbles.<sup>3,93</sup> Recently, self-templating approaches based on such principles as the Kirkendall effect,<sup>93</sup> Ostwald ripening,<sup>94</sup> galvanic replacement,<sup>95</sup> and chemical etching,<sup>3</sup> have been adopted, where templates simultaneously sacrifice during the formation of hollow structures.

**Template-Based Synthesis.** Template-based methods offer many important advantages, including narrow size distribution products with well-defined structural features.<sup>16</sup> However, there are some drawbacks such as difficulties in a complete removal of the template and in the limited ability to conduct large-scale syntheses. Commonly, the removal of the template involves calcination at high temperature (e.g., to remove carbon or polystyrene spheres), or chemical dissolution (e.g., use of hydrofluoric acid to remove silica templates), which may result in collapse of some fraction of the hollow structures.<sup>96,97</sup> Therefore, it is highly desirable to develop new strategies for synthesizing hollow  $\text{SnO}_2$  nanostructures. Ding et al.<sup>98</sup> reported the hierarchical assembly of  $\text{SnO}_2$  nanosheets into hollow spheres by using the sulfonated gel matrix of polystyrene

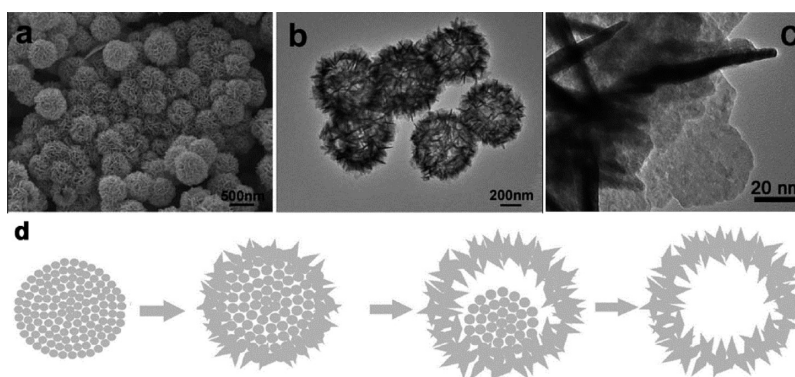


**Figure 3.** (a) SEM and (b) TEM images of hollow  $\text{SnO}_2$  spheres assembled from 2D nanosheets (shown in panel c). (Reproduced with permission from ref 98, Copyright 2011, Royal Society of Chemistry, London.) (d) Schematic illustration of the growth process of the hollow nanostructure by consuming the core material via the Ostwald ripening process. (Reproduced with permission from ref 70, Copyright 2010, American Chemical Society, Washington, DC.)

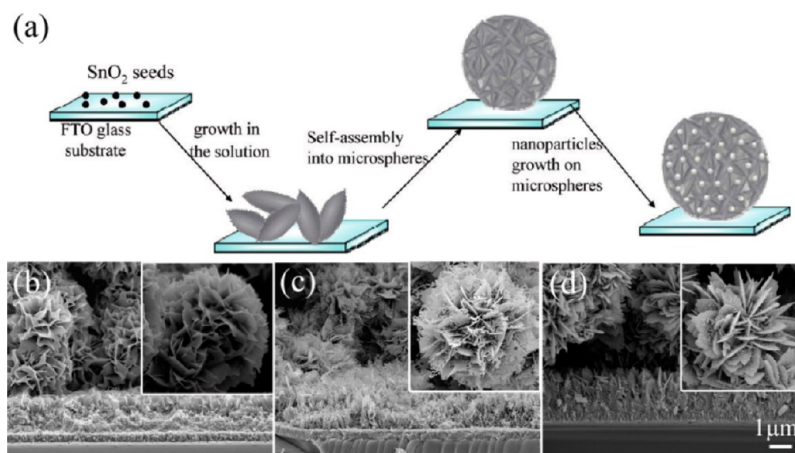


**Figure 4.** (a) Schematic illustration of the growing process of hierarchical SnO<sub>2</sub> microspheres on a FTO glass substrate. (Reproduced with permission from ref 104, Copyright 2010, American Chemical Society, Washington, DC.) (b–d) SEM images of hierarchical SnO<sub>2</sub> nanostructured bilayer films directly grown on FTO glass substrates under varying synthetic conditions (author's own unpublished data). Insets in panels b–d present the morphology of representative hierarchical SnO<sub>2</sub> nanoflowers from the top layer (size in the range of 2–5 μm). The scale bar in panel d is the same for panels b and c.

hollow spheres as templates (see Figures 3a–c). The sulfonated polystyrene spheres with hydrophilic and negative functional groups facilitate the adsorption of the positively charged precursor Sn<sup>2+</sup> ions. The strategy allows the in situ growth of SnO<sub>x</sub> ( $x = 1$  or 2) nanosheets within the polymer gel shell, which subsequently develop into a hierarchical structure.

Yan et al.<sup>99</sup> reported the synthesis of hierarchical SnO<sub>2</sub> hollow spheres with shells constructed by two layers of tetragonal prism nanorod arrays, formed on the surface of self-generated NO bubbles in the aqueous solution. Such a template method involves no further heat treatment, which is promising in the design of the hollow structures. Wang et al.<sup>68</sup> demonstrated that the formation of SnO<sub>2</sub> nanorods assembled into hollow microspheres relies on the use of (CH<sub>2</sub>)<sub>6</sub>N<sub>4</sub>, which is a nontoxic, water-soluble, nonionic amine able to hydrolyze and produce NH<sub>3</sub> gas under the hydrothermal treatment, serving as the soft template to prepare the hollow structure.

**Template-Free Synthesis.** Ostwald ripening process has been widely utilized in the formation of hollow structures,<sup>100</sup> which is a coarsening process of consuming smaller particles to grow into bigger particles. The formation of hollow interiors in the secondary aggregates containing nanoscale primary particles is largely dependent on their packing arrangement. If the primary particles in the outer part of the aggregates are larger or packed in a denser manner than those in the inner part, they grow at the expense of those in the core, resulting in the hollow interiors. Moreover, the loose packing of primary particles is beneficial for their dissolution during the hydrothermal/solvothermal reaction. Lou et al.<sup>64</sup> prepared hollow SnO<sub>2</sub> spheres (~200 nm in size) with shells composed of 0D nanoparticles and suggested solid evacuation by Ostwald ripening as the major driving mechanism. Solid evacuation is a ripening process, in which crystallites located in the central regions dissolve and relocate on the surfaces of the aggregates, leaving behind hollow structures.<sup>101,102</sup>

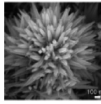
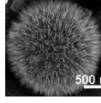
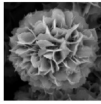
Yin and co-workers<sup>73</sup> reported a template-free route to prepare hierarchical SnO<sub>2</sub> hollow architectures self-assembled from 2D nanosheets via hydrothermal treatment of the SnSO<sub>4</sub> suspension in deionized water, without the presence of any surfactants or morphology-controlling agents. Hydrolysis and oxidation of Sn<sup>2+</sup> at the initial reaction stage result in the

formation of metastable SnO<sub>2</sub> nanocrystallites, which are prone to form aggregated SnO<sub>2</sub> spheres to lower their high surface energy. At the subsequent stage, SnO<sub>2</sub> nanosheets grew on the surface of spheres by consuming core materials via the Ostwald ripening process (see Figure 4d). In a similar approach, Liu et al.<sup>69</sup> prepared hierarchical urchin-like hollow SnO<sub>2</sub> nanostructures, where 1D nanorod units grew by consuming initially spherical aggregates.

We reported the growth of hierarchical SnO<sub>2</sub> microspheres with either a solid or hollow interior composed of aligned conelike SnO<sub>2</sub> nanoplates, using SnCl<sub>4</sub>·5H<sub>2</sub>O as the tin source, and either NH<sub>4</sub>F or NaF as morphology-controlling agents, respectively.<sup>103</sup> The solid spheres preferentially recrystallized starting from the cores and grew by consuming adjacent smaller particles, while the hollow spheres preferentially recrystallized starting from outer shells and grew by consuming the entrapped core materials via the mechanism of solid evacuation. The different growth paths were attributed to the fluoride-dependent crystallinity of the primary aggregated nanoparticles.<sup>103</sup>

**2.4. Growth of Hierarchical SnO<sub>2</sub> Nanostructures on Substrates.** Direct growth of nanostructured metal oxide films on diverse substrates has attracted considerable research interest, greatly as a means to create direct electron pathways facilitating the transportation and separation of photogenerated carriers, which is particularly important for both photovoltaic cells and photocatalytic hydrogen production.<sup>56,105–108</sup> Several methods have been developed to fabricate oriented SnO<sub>2</sub> arrays on a variety of substrates.<sup>106,109–121</sup> Polycrystalline SnO<sub>2</sub> nanotube arrays were grown on opaque substrates such as silicon, stainless steel, and copper foils, using ZnO nanorod arrays as sacrificial templates.<sup>112,117</sup> Shinde et al.<sup>113,116</sup> reported the low-temperature wet chemical synthesis of SnO<sub>2</sub> nanowall arrays on transparent FTO substrates, making use of suitable organic additives, while Krishnamoorthy et al.<sup>111</sup> suggested the growth of polycrystalline SnO<sub>2</sub> nanowire arrays on FTO substrates assisted by the electrospinning of polymers. Wang et al.<sup>104</sup> suggested the preparation of SnO<sub>2</sub> films on FTO substrates using precoated SnO<sub>2</sub> as seed layers, via hydrothermal methods using SnCl<sub>4</sub>, NH<sub>4</sub>F, and acetylacetone (see Figure 4a), where cooperative effects of all ingredients were

Table 3. Representative Examples of Doping Strategies for SnO<sub>2</sub> Hierarchical Nanostructures

SEM image	Constituting units	Typical synthesis	Ref.
	Zn-doped SnO <sub>2</sub> nanorods	Precursors: 1.0mmol SnCl <sub>4</sub> , 15.0 mmol NaOH; H <sub>2</sub> O/ethanol (30mL, 1:1, v/v); 0.02mmol Zn(CH <sub>3</sub> COO) <sub>2</sub> ·2H <sub>2</sub> O (Zn/Sn=2 at.%) Procedure: hydrothermal method, 180 °C for 24 h	46
	Zn-doped SnO <sub>2</sub> nanowires	Precursors: 0.21g SnCl <sub>4</sub> ·5H <sub>2</sub> O, 0.29g NaOH, 0.216g CO(NH <sub>2</sub> ) <sub>2</sub> ; H <sub>2</sub> O/ethylenediamine (30 mL, 1:1, v/v); 0.612g C <sub>12</sub> H <sub>22</sub> O <sub>14</sub> Zn (Zn/Sn=4.95 at.%) Procedure: hydrothermal method, 200 °C for 24 h	47
	Zn-doped SnO <sub>2</sub> nanocones	Precursors: 0.526g SnCl <sub>4</sub> ·5H <sub>2</sub> O, 0.6g NaOH, 0.6g CTAB, 0.2g HMT, H <sub>2</sub> O/methanol (40 mL, 1:1, v/v), Zn(NO <sub>3</sub> ) <sub>2</sub> ·6H <sub>2</sub> O (Zn/Sn=6.7~20 at. %) Procedure: hydrothermal method, 200 °C for 24 h	48
	Sn <sup>2+</sup> -doped SnO <sub>2</sub> nanosheets	Precursors: 30mL H <sub>2</sub> O, 0.57g NaF, 0.65g SnCl <sub>2</sub> ·2H <sub>2</sub> O, Sn <sup>2+</sup> -self-doping Procedure: hydrothermal method, 180 °C for 6 h	75

responsible for the formation of hierarchical SnO<sub>2</sub> microspheres consisting of nanosheets and nanoparticles. In our related ongoing work,<sup>122</sup> we demonstrated the direct growth of SnO<sub>2</sub> bilayer films on FTO substrates, consisting of upstanding SnO<sub>2</sub> nanosheet array bottom layer and hierarchical SnO<sub>2</sub> nanoflower top layer, via the hydrothermal method using SnCl<sub>2</sub> and NaF (see Figures 4b–d). The morphology of the layers could be controlled by adjusting the hydrothermal reaction time and the post-preparative thermal treatment. The FTO itself serves as a seed layer, and the method can be generally applied to other substrates via the preplanting of SnO<sub>2</sub> seeds. Subunit sizes of such SnO<sub>2</sub> films comparable to the wavelength of light can enhance the light harvesting efficiency via the scattering effects,<sup>47,123</sup> so that their deposition on conductive substrates is often beneficial for the potential applications in displays and solar cells.

**2.5. Doped Hierarchical SnO<sub>2</sub> Nanostructures.** The doping of oxide nanomaterials is a general approach to tailor their electrical and optical properties.<sup>46–48,124</sup> In relation to hierarchical SnO<sub>2</sub> nanostructures, doping with Zn<sup>2+</sup> ions has been actively pursued by several groups in order to improve their performance in dye-sensitized solar cells<sup>46,47</sup> and gas sensors.<sup>125</sup> According to the literature reports,<sup>38</sup> Sn(IV) readily forms Sn(OH)<sub>6</sub><sup>2-</sup> ions in highly alkaline solution, which further undergo decomposition to produce SnO<sub>2</sub> nuclei. Upon introduction of Zn<sup>2+</sup> into the reaction mixture, different morphologies of Zn-doped 1D and 2D building units of hierarchical SnO<sub>2</sub> nanostructures can be formed, affected by the nature of zinc precursors, organic additives and solvents as exemplified in Table 3. Dou et al.<sup>46</sup> produced spherical hierarchical SnO<sub>2</sub> nanoflowers loosely constructed by rodlike nanocones with growth orientation along the [11 $\bar{2}$ ] direction at a low level Zn doping, which is the same morphology as for pristine SnO<sub>2</sub> nanorods.<sup>38</sup> Li et al.<sup>47</sup> reported Zn-doped SnO<sub>2</sub> nanostructures composed of dense nanowires with growth orientation along the [101] direction, prepared in water/ethylenediamine as a binary solvent mixture. Sun et al.<sup>48</sup> proposed hydrothermal synthesis of Zn-doped SnO<sub>2</sub> hierarchical architectures constructed from nanocones whose morphology changed from an urchin-like structure to “weave cloth”-like

one with the increase of the concentration of Zn<sup>2+</sup> ions (Figure 5a–d). Their growth mechanism is illustrated by the scheme

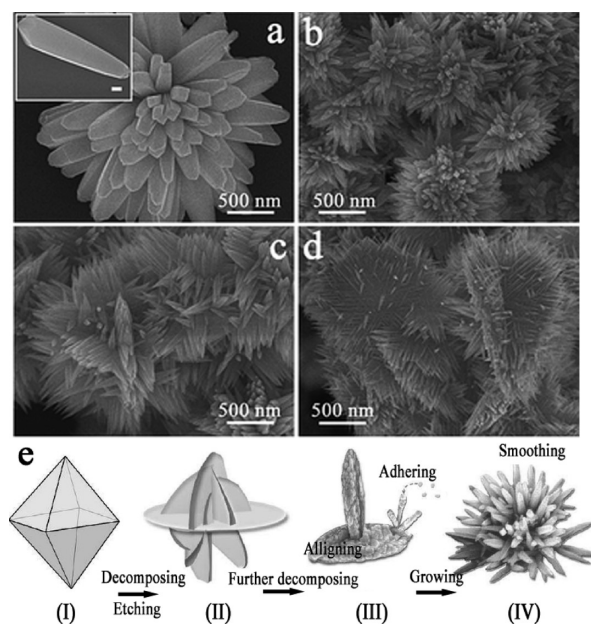


**Figure 5.** SEM images of Zn-doped SnO<sub>2</sub> hierarchical structures grown under different ratios  $R$  ( $R = [\text{Zn}^{2+}]/[\text{Sn}^{4+}]$ ) of introduced Zn dopant: (a)  $R = 0$ , (b)  $R = 1/15$ , (c)  $R = 2/15$ , (d)  $R = 3/15$ . The inset in panel (a) shows an enlarged image of constituting 2D nanoplate with a scale bar of 100 nm. (Reproduced with permission from ref 48, Copyright 2012, Royal Society of Chemistry, London.) (e) Schematic illustration of the morphology evolution of the Zn-doped SnO<sub>2</sub> nanostructures. (Reproduced with permission from ref 46, Copyright 2011, American Chemical Society, Washington, DC.)

presented in Figure 5e. At the initial reaction stage (I), Sn(OH)<sub>6</sub><sup>2-</sup> ions are formed due to the high molar ratio of OH<sup>-</sup> to Sn<sup>4+</sup>, parts of which then react with Zn<sup>2+</sup> and produce ZnSn(OH)<sub>6</sub> bipyramids under the hydrothermal condition. At stage II, because of the etching effect of additional OH<sup>-</sup>, ZnSn(OH)<sub>6</sub> bipyramids are decomposed into Zn(OH)<sub>4</sub><sup>2-</sup> and

$\text{Sn}(\text{OH})_6^{2-}$  along the bipyramid surface and form some amount of Zn-doped  $\text{SnO}_2$  nanocrystals in solution, while the residual structure decomposes into Zn-doped  $\text{SnO}_2$  plates and  $\text{Zn}_2\text{SnO}_4$ . At stage III, Zn-doped  $\text{SnO}_2$  nanocrystals from solution attach onto the surface of the plates, aligning themselves into nanowires with rough surfaces. At the same time,  $\text{Zn}_2\text{SnO}_4$  further react with  $\text{Sn}(\text{OH})_6^{2-}$  and form more Zn-doped  $\text{SnO}_2$  nanocrystals in solution. At stage IV, the rough nanowires continue to grow and smoothen into the thorns of the resulting Zn-doped  $\text{SnO}_2$  hierarchical nanostructure.

The doping of  $\text{SnO}_2$  nanostructures with elements other than Zn, such as In and Ti, has been also reported.<sup>124,126</sup> We have recently developed the synthesis of 3D hierarchical  $\text{SnO}_2$  nanoflowers using NaF as the morphology-controlling agent and  $\text{SnCl}_2$  as the tin source, which resulted in the simultaneous  $\text{Sn}^{2+}$  self-doping of  $\text{SnO}_2$  nanostructures, leading to the formation of tunable oxygen vacancies bandgap states and the corresponding shifting in the semiconductor Fermi levels, and extended absorption in the visible spectral range.<sup>75</sup> This particular synthesis can be modified via the introduction of titanate ( $\text{H}_2\text{Ti}_3\text{O}_7$ ) nanowires, serving as both sacrificial templates and the Ti dopant source.<sup>127</sup> In the latter case, quasi-1D hierarchical  $\text{SnO}_2$  nanowires composed of Ti-doped  $\text{SnO}_2$  nanosheets were obtained. The self-doping and assembly of  $\text{SnO}_2$  nanosheets on the nanowires were attributed to the excessive fluoride, which inhibits the hydrolysis of  $\text{SnCl}_2$ , thus causing heterogeneous nucleation to occur preferentially on the titanate nanowires. Simultaneously, titanate nanowires dissolve into  $\text{Ti}^{4+}$  species under the etching effect of self-generated HF, which allows for spontaneous Ti doping and formation of  $\text{SnO}_2$  nanosheets via hydrolysis, dehydration, and crystallization under hydrothermal conditions.  $\text{Ti}^{4+}$  species were uniformly distributed within the  $\text{SnO}_2$  nanosheets by substitution of Sn sites at a high level (Ti/Sn ratio of 15%–20%) and with no phase separation.

### 3. APPLICATIONS OF HIERARCHICAL $\text{SnO}_2$ NANOSTRUCTURES

**3.1. Lithium-Ion Batteries.**  $\text{SnO}_2$  has been considered to be one of the most promising anode materials for high-performance lithium-ion batteries,<sup>2,3,14,16,39,64,73,128–130</sup> because of its high theoretical specific storage capacity ( $782 \text{ mA h g}^{-1}$ ), compared with currently commercially used graphite ( $372 \text{ mA h g}^{-1}$ ).<sup>64</sup> The mechanism of lithium storage for  $\text{SnO}_2$  is based on the alloying/dealloying processes, which are the intrinsic driving force for the electrochemical activity:<sup>131,132</sup>



However, large volume expansion induced by the lithiation/delithiation process often causes pulverization, resulting in severe internal strain, cracking, and blocking of the electrical contact pathways in the electrodes, which leads to their rapid deterioration and low retention of the electrical capacity.<sup>2,11,133</sup> To overcome these problems, several strategies have been adopted to optimize the structure and composition as well as the morphology of  $\text{SnO}_2$ -based materials, which include the use of hierarchical hollow or mesoporous  $\text{SnO}_2$  architectures assembled from 0D nanoparticles,<sup>13,14,64</sup> 1D nanorods and nanowires,<sup>92,103</sup> 2D nanosheets,<sup>41,73</sup> and carbon-coated  $\text{SnO}_2$ .<sup>39,134,135</sup>

Wu et al.<sup>41</sup> reported that hierarchical  $\text{SnO}_2$  nanostructures constructed from 2D nanosheets exhibit superior reversible

capacities (discharge capacity of  $516 \text{ mA h g}^{-1}$ ) and improved cyclic capacity retention (80%) after 50 cycles at a current rate of  $400 \text{ mA g}^{-1}$ , which is much higher than that of commercial  $\text{SnO}_2$  nanoparticles used for comparison ( $286 \text{ mA g}^{-1}$ , 48% retention). They ascribed this to its stable porous structure, which is due to the effective prevention of dense aggregation of constituting nanosheets. The high porosity of such hierarchical structures, short transport paths of  $\text{SnO}_2$  nanosheets, and the interconnections between the individual building blocks render them promising candidates as anode materials for lithium-ion batteries. Jiang et al.<sup>92</sup> reported that hierarchical  $\text{SnO}_2$  nanostructures with a carbon coating ( $\text{SnO}_2$ -C composite) exhibit improved cycling performance with a reversible capacity of  $\sim 700 \text{ mA h g}^{-1}$  after 20 cycles, which is much higher than that of bare  $\text{SnO}_2$  without a carbon coating ( $\sim 200 \text{ mA h g}^{-1}$ ). The carbon coating helps to maintain the integrity of active particles, leading to a stabilized surface toward the formation of solid electrolyte interface thin films, thus enhancing the initial Coulombic efficiency, specific capacity, and cycling performance of electrode materials. Besides, the carbon coating layer acts as a buffer to relieve the strain produced by the volume variations during Li-Sn alloying-dealloying processes, according to eq 6.

$\text{TiO}_2$  is yet another widely investigated anode material for lithium-ion batteries, because of its long cycle life and high rate capability, as well as its low cost and minimum environment impact.<sup>15,136,137</sup> However,  $\text{TiO}_2$  has a much lower theoretical capacity ( $170 \text{ mA h g}^{-1}$ ) than  $\text{SnO}_2$  ( $782 \text{ mA h g}^{-1}$ ) and graphite ( $372 \text{ mA h g}^{-1}$ ). One significant advantage of  $\text{TiO}_2$  is its ability to undergo fast discharging/charging (higher power) processes without compromising its structure and energy storage capacity.<sup>15</sup> To take advantage of both the high capacity of  $\text{SnO}_2$  and the high rate performance of  $\text{TiO}_2$  anodes, Ti doping of  $\text{SnO}_2$  nanostructures offers a suitable strategy. We reported improved electrochemical performance of quasi-1D hierarchical Ti-doped  $\text{SnO}_2$  nanostructures composed of 2D nanosheets, with a discharge capacity of  $\sim 500 \text{ mA h g}^{-1}$  and 74% retention after 20 cycles at a constant current density of  $250 \text{ mA g}^{-1}$ , which has been attributed to the diluted surface Sn atoms after Ti substitution, alleviating volume expansion.<sup>127</sup> It is thus anticipated that future anode materials with better lithium storage properties can be obtained by design, while combining Sn-based and Ti-based components.

**3.2. Gas Sensors.** The working principle of oxide semiconductor gas sensors is based on the significant resistance change upon exposure to detecting gases. For *n*-type  $\text{SnO}_2$ , an electron-depletion layer forms on the semiconductor surface, because of the chemisorbed oxygen, resulting in the structures of semiconducting cores and resistive shells.<sup>1,138</sup> Upon exposure to reductive gases, the latter are oxidized by negatively charged oxygen species adsorbed on the  $\text{SnO}_2$  surface, and the conductivity of sensors thus increases as more electrons are produced by the oxidation reactions. To improve sensitivity of gas sensors, it is important to develop active materials with large surface areas and large porosity, ensuring the easy access of analyte gases. In dense nanoparticle aggregates, the gas response is limited by small pore sizes, while hierarchical nanostructures with open porous structure offer advantages both in terms of high surface areas and fast gas response. In general, the gas-sensing properties of hierarchical structures are largely determined by the dimensions and packing arrangement of building blocks, and, thus, the resultant porosity. The periodic hierarchical assembly of  $\text{SnO}_2$  building blocks provides

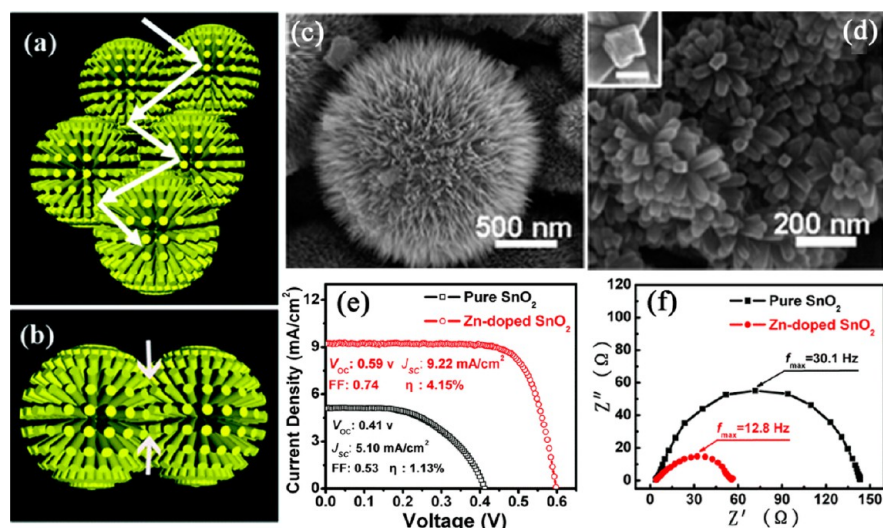


**Figure 6.** (a) Schematic illustration of multiple light reflection and scattering favored by nanowire-textured surface and the microspherical structure of the Zn-doped SnO<sub>2</sub> echinus. (b) Schematic illustration of intersectional contacts between the nanowires of neighboring spheres, increasing the transport channel of the injected electrons through the adjacent spheres. SEM images of (c) Zn-doped SnO<sub>2</sub> with high surface area and (d) pure SnO<sub>2</sub> with an inset showing enlarged compact building block of the latter (scale bar = 50 nm). (e) Current–voltage (*I*–*V*) curves for solar cells based on the pure SnO<sub>2</sub> and Zn-doped SnO<sub>2</sub> photoanodes. (f) Nyquist plots of electrochemical impedance spectra of the pure SnO<sub>2</sub> and Zn-doped SnO<sub>2</sub> photoanodes. (Reproduced with permission from ref 47, Copyright 2012, Royal Society of Chemistry, London.)

a large surface area for the interfacial chemical reactions, as well as effective diffusion of target gases toward the gas-sensing interface. Highly porous films constructed by hierarchical nanostructures also offer additional possibilities for further modifications, such as metal loading to improve the sensitivity and selectivity of the resulting gas sensors.

Jiang et al.<sup>92</sup> studied the gas-sensing properties of hierarchical SnO<sub>2</sub> nanostructures constructed from porous nanowires (as shown in Figure 2), which provide broad pore size distribution ranging from <2 nm to >50 nm, and demonstrated their remarkably high sensitivity and reversibility for H<sub>2</sub> and CO sensing with detection limit of 5 ppm. The sensitivity of sensors showed a good linearity with the concentration of target gas and the sensitivity toward H<sub>2</sub> molecules was higher than that for CO, which was attributed to the effects of steric hindrance on the diffusion and accessibility of the target gases to the deeper regions of SnO<sub>2</sub> layers in view of the different molecular sizes of H<sub>2</sub> and CO. Our group demonstrated that Sn<sup>2+</sup>-doped hierarchical SnO<sub>2</sub> nanostructures possess higher sensitivity to oxidizing gas NO<sub>2</sub>, rather than to reductive vapors such as acetone and ethanol.<sup>75</sup> The Sn<sup>2+</sup> self-doping of SnO<sub>2</sub> nanoflowers leads to the formation of tunable oxygen vacancy bandgap states and the corresponding shifting in the semiconductor Fermi levels, and it increases the density of states of these Sn<sup>2+</sup>-doped SnO<sub>2</sub>, which gives rise to enhanced charge transfer, which is responsible for the high sensing response and selectivity toward NO<sub>2</sub>.

Besides doping, loading SnO<sub>2</sub> nanostructures with noble-metal particles provides another useful strategy to improve their gas-sensing properties. Sun et al.<sup>66</sup> showed that the response of hierarchical Pd-loaded SnO<sub>2</sub> nanorods to 1000 ppm butanone was ~10 times higher than that of a sensor based on unloaded SnO<sub>2</sub>. Besides, it exhibited much higher selectivity to butanone against other testing gases, with a sensitivity 2.3 times higher than the second highest value for ethanol. The enhanced gas response and selectivity were ascribed to “electronic” and “chemical” mechanisms. The former suggests that the oxidized state (PdO) of Pd nanoparticles captures electrons from SnO<sub>2</sub>,

resulting in the formation of strongly depletive space charge layer near the Pb/SnO<sub>2</sub> interface. When the sensor was exposed to the target gas, PdO was reduced and released the trapped electrons to SnO<sub>2</sub> nanorods, giving rise to the relaxing space charge layer, and a large increase in the gas response. “Chemical mechanism” suggests that the test gas is activated and spills over by the noble-metal additive, facilitating the chemical reaction between the gas and the adsorbed oxygen on the SnO<sub>2</sub> surface. This mechanism is well-established in the catalysis and is known as the “spillover effect”.<sup>66,139</sup> The great enhancement of the sensitivity to butanone was attributed to the catalytic effect of PdO, breaking butanone into active radicals, which react with the surface-adsorbed oxygen ions. As a result, more trapped electrons are released back to the conduction band of SnO<sub>2</sub>.

**3.3. Sensitized Solar Cells.** SnO<sub>2</sub> in its bulk form is a wide-bandgap (3.6 eV) semiconducting oxide, which has an electron mobility (100–200 cm<sup>2</sup> V<sup>-1</sup> s<sup>-1</sup>) that is much higher than that of anatase TiO<sub>2</sub> (0.1–1 cm<sup>2</sup> V<sup>-1</sup> s<sup>-1</sup>) or porous TiO<sub>2</sub> (10<sup>-2</sup> cm<sup>2</sup> V<sup>-1</sup> s<sup>-1</sup>).<sup>33,46,123</sup> Its more-negative conduction band minimum, 0.3 eV lower than that of anatase TiO<sub>2</sub>, facilitates electron transfer from the low-bandgap sensitizers such as PbS quantum dots, and dyes with lower-lying lowest unoccupied molecular orbitals (LUMOs) such as several perylenes, so that light harvesting in the near-infrared spectral region could be significantly enhanced. Therefore, nanostructured SnO<sub>2</sub> is a potentially promising photoanode material that allows for efficient charge collection, and it has been extensively studied in dye-sensitized solar cells (DSSCs)<sup>31,32,46,140,141</sup> and also in quantum-dot sensitized solar cells<sup>33</sup> configurations. The limitations of SnO<sub>2</sub>-based DSSCs are the relatively weak adsorption of the dyes with acidic anchoring groups, and the recombination of conduction band electrons with the oxidized dye.<sup>46,142</sup> Another limitation of SnO<sub>2</sub>-based DSSCs is their low open-circuit voltage (*V*<sub>oc</sub>) when coupled with iodide/triiodide redox couple (~0.45 V),<sup>143</sup> which can be improved by coating with isolating oxides such as TiO<sub>2</sub>,<sup>140</sup> ZnO, Al<sub>2</sub>O<sub>3</sub>, or MgO.<sup>30,144</sup>

For a high-efficiency DSSCs, the SnO<sub>2</sub> photoanode requires both a high surface area with well-accessed pores for loading of light harvesting dyes, and, at the same time, a densely packed microstructure offering pathways for fast electron transport (see Figure 6b). Hierarchical nanostructures assembled from the primary building blocks can maintain the high surface area and, at the same time, offer larger pores for dye loading, thus enhancing the light-harvesting ability of the photoanode. Moreover, hierarchical nanostructures with subunit sizes comparable to the wavelength of visible light can enhance the light-harvesting efficiency via the scattering effects,<sup>47,123</sup> which increases the light transport length within the photoanode film (Figure 6a) and thus the probability of photon absorption by photosensitizers. This can be combined with band engineering by doping, which has been recently demonstrated by Li et al.<sup>47</sup> for Zn-doped hierarchical SnO<sub>2</sub> spheres (see Figures 6c and 6d). Zn doping induces a negative shift in the flat-band potential and contributes to the improved  $V_{oc}$ ; at the same time, it increases the isoelectric point of the surface, which facilitates the adsorption of dyes through their anchoring acidic carboxyl groups. As a result, Zn-doped SnO<sub>2</sub> photoanodes exhibit higher open-circuit photovoltages, larger short-circuit currents, longer electron lifetimes, and increased dye loading than their undoped SnO<sub>2</sub> counterparts, with conversion efficiencies of up to 4.15%, which is an almost 3-fold improvement, compared to undoped SnO<sub>2</sub> photoanodes (see Figure 6e). Dou et al.<sup>46</sup> also reported improved photovoltaic performance of Zn-doped SnO<sub>2</sub> photoanodes with  $V_{oc} = 0.78$  V and an overall power conversion efficiency of 3.0%, which has been further increased to 6.78% as a result of treatment with TiCl<sub>4</sub>. Electrochemical impedance spectroscopy demonstrated that Zn-doped SnO<sub>2</sub> photoanodes have higher intrinsic electron mobility than the conventional SnO<sub>2</sub> electrodes (Figure 6f), which favors the fast charge transport. Thus far, both surface and electronic modification of hierarchical SnO<sub>2</sub> photoanode films are promising strategies to improve the energy conversion efficiency of the resulting solar cells.

#### 4. CONCLUSIONS AND OUTLOOK

In this review, we discussed the synthesis of hierarchical SnO<sub>2</sub> nanostructures combined with the morphology engineering, in terms of dimension and facet control of their constituting building blocks and the creation of porous and hollow structures, as well as their modification by doping and loading with other elements (such as Zn<sup>2+</sup>, Sn<sup>2+</sup>, Ti<sup>4+</sup>, and Pd). Reaction parameters such as the chemical state of the tin precursors (Sn(IV) vs Sn(II) salts), concentration, additives, and solvents play an important role in this respect. As anode materials, hierarchical SnO<sub>2</sub> nanostructures with porous and hollow structures demonstrate superior lithium storage properties, and the titanium doping of SnO<sub>2</sub> can improve their cycle performance. In the gas sensing, hierarchical SnO<sub>2</sub> nanostructures with mesoporous structure facilitate gas diffusion within the pores, which results in a faster and higher response, and their sensitivity can be improved by ion doping or noble-metal loading. As photoanode materials for sensitized solar cells, Zn-doped hierarchical SnO<sub>2</sub> nanostructures show enhanced photovoltaic performance, because of the combined advantages of high surface area for light absorbers, light scattering and increased light utilization, and improved electron-transport properties. Therefore, hierarchical SnO<sub>2</sub> nanostructures with a proper design of constituting building units, combined with advantages offered by doping possess several advanced physical

and chemical properties, which are important for a variety of energy and environment applications.

Although significant progress has been made in the synthesis of hierarchical SnO<sub>2</sub> nanostructures, further efforts are still required to better understand the interactions between building units, which are still unclear but crucial for the design of hierarchical structures in desired ways and the optimization of their gas sensing, lithium storage, and energy conversion performance. The introduction of components with different chemical compositions, which can be conveniently realized by doping, can generate advantageous characteristics, compared to their pure-phase counterparts. Flexible facet engineering of two-dimensional (2D) SnO<sub>2</sub> nanosheet building blocks is particularly important in exploiting their surface-dependent properties for catalytic and gas-sensor applications, while it is still challenging in terms of the large-scale, high-yield synthesis of SnO<sub>2</sub> nanocrystals with a large percentage of specific facets exposed. We hope that the present review will stimulate further development of hierarchical SnO<sub>2</sub> nanostructures, as well as advance their applications to meet the current and future environment- and energy-related demands.

#### AUTHOR INFORMATION

##### Corresponding Author

\*E-mail: andrey.rogach@cityu.edu.hk

##### Notes

The authors declare no competing financial interest.

#### ACKNOWLEDGMENTS

This work was supported by City University of Hong Kong, through Applied Research Grant No. 9667067.

#### REFERENCES

- (1) Han, X.; Jin, M.; Xie, S.; Kuang, Q.; Jiang, Z.; Jiang, Y.; Xie, Z.; Zheng, L. *Angew. Chem., Int. Ed.* **2009**, *48*, 9180–9183.
- (2) Wang, C.; Zhou, Y.; Ge, M.; Xu, X.; Zhang, Z.; Jiang, J. *J. Am. Chem. Soc.* **2009**, *132*, 46–47.
- (3) Wang, Z.; Luan, D.; Boey, F. Y.; Lou, X. W. *J. Am. Chem. Soc.* **2011**, *133*, 4738–4741.
- (4) Yang, H. G.; Sun, C. H.; Qiao, S. Z.; Zou, J.; Liu, G.; Smith, S. C.; Cheng, H. M.; Lu, G. Q. *Nature* **2008**, *453*, 638–641.
- (5) Chen, X.; Liu, L.; Yu, P. Y.; Mao, S. S. *Science* **2011**, 746–750.
- (6) Pan, Z. W.; Dai, Z. R.; Wang, Z. L. *Science* **2001**, *291*, 1947–1949.
- (7) Xu, X.; Zhuang, J.; Wang, X. *J. Am. Chem. Soc.* **2008**, *130*, 12527–12535.
- (8) Ding, S.; Chen, J. S.; Lou, X. W. *Adv. Funct. Mater.* **2011**, *21*, 4120–4125.
- (9) Wen, Z.; Wang, Q.; Zhang, Q.; Li, J. *Adv. Funct. Mater.* **2007**, *17*, 2772–2778.
- (10) Zhang, H.-X.; Feng, C.; Zhai, Y.-C.; Jiang, K.-L.; Li, Q.-Q.; Fan, S.-S. *Adv. Mater.* **2009**, *21*, 2299–2304.
- (11) Ding, S.; Luan, D.; Boey, F. Y. C.; Chen, J. S.; Lou, X. W. *Chem. Commun.* **2011**, 47, 7155–7157.
- (12) Chen, G.; Wang, Z.; Xia, D. *Chem. Mater.* **2008**, *20*, 6951–6956.
- (13) Demir-Cakan, R.; Hu, Y. S.; Antonietti, M.; Maier, J.; Titirici, M. M. *Chem. Mater.* **2008**, *20*, 1227–1229.
- (14) Deng, D.; Lee, J. Y. *Chem. Mater.* **2008**, *20*, 1841–1846.
- (15) Chen, J. S.; Archer, L. A.; Lou, X. W. *J. Mater. Chem.* **2011**, *21*, 9912–9924.
- (16) Ding, S. J.; Chen, J. S.; Qi, G. G.; Duan, X. N.; Wang, Z. Y.; Giannelis, E. P.; Archer, L. A.; Lou, X. W. *J. Am. Chem. Soc.* **2011**, *133*, 21–23.

- (17) Kravchuk, K.; Protesescu, L.; Bodnarchuk, M.; Krumeich, F.; Yarema, M.; Walter, M.; Guntlin, C.; Kovalenko, M. *J. Am. Chem. Soc.* **2013**, *135*, 4199–4202.
- (18) Lu, G.; Ocola, L. E.; Chen, J. *Adv. Mater.* **2009**, *21*, 2487–2491.
- (19) D'Arienzo, M.; Armelao, L.; Cacciamani, A.; Mari, C. M.; Polizzi, S.; Ruffo, R.; Scotti, R.; Testino, A.; Wahba, L.; Morazzoni, F. *Chem. Mater.* **2010**, *22*, 4083–4089.
- (20) Gyger, F.; Hubner, M.; Feldmann, C.; Barsan, N.; Weimar, U. *Chem. Mater.* **2010**, *22*, 4821–4827.
- (21) Zhang, J.; Wang, S. R.; Xu, M. J.; Wang, Y.; Xia, H. J.; Zhang, S. M.; Guo, X. Z.; Wu, S. H. *J. Phys. Chem. C* **2009**, *113*, 1662–1665.
- (22) Wang, Y.; Jiang, X.; Xia, Y. *J. Am. Chem. Soc.* **2003**, *125*, 16176–16177.
- (23) Martinez, C. J.; Hockey, B.; Montgomery, C. B.; Semancik, S. *Langmuir* **2005**, *21*, 7937–7944.
- (24) Maiti, A.; Rodriguez, J. A.; Law, M.; Kung, P.; McKinney, J. R.; Yang, P. *Nano Lett.* **2003**, *3*, 1025–1028.
- (25) Göpel, W.; Schierbaum, K. D. *Sens. Actuators, B* **1995**, *26*, 1–12.
- (26) Xu, J. Q.; Wang, D.; Qin, L. P.; Yu, W. J.; Pan, Q. Y. *Sens. Actuators, B* **2009**, *137*, 490–495.
- (27) Qian, J. F.; Liu, P.; Xiao, Y.; Jiang, Y.; Cao, Y. L.; Ai, X. P.; Yang, H. X. *Adv. Mater.* **2009**, *21*, 3663–3667.
- (28) Prasittichai, C.; Hupp, J. T. *J. Phys. Chem. Lett.* **2010**, *1*, 1611–1615.
- (29) Snaith, H. J.; Stavrinadis, A.; Docampo, P.; Watt, A. A. R. *Sol. Energy* **2011**, *85*, 1283–1290.
- (30) Kay, A.; Grätzel, M. *Chem. Mater.* **2002**, *14*, 2930–2935.
- (31) Ramasamy, E.; Lee, J. *J. Phys. Chem. C* **2010**, *114*, 22032–22037.
- (32) Snaith, H. J.; Ducati, C. *Nano Lett.* **2010**, *10*, 1259–1265.
- (33) Hossain, M. A.; Jennings, J. R.; Koh, Z. Y.; Wang, Q. *ACS Nano* **2011**, *5*, 3172–3181.
- (34) Wrighton, M. S.; Morse, D. L.; Ellis, A. B.; Ginley, D. S.; Abrahamson, H. B. *J. Am. Chem. Soc.* **1976**, *98*, 44–48.
- (35) Long, J.; Xue, W.; Xie, X.; Gu, Q.; Zhou, Y.; Chi, Y.; Chen, W.; Ding, Z.; Wang, X. *Catal. Commun.* **2011**, *16*, 215–219.
- (36) Zhang, H.; Hu, C. *Catal. Commun.* **2011**, *14*, 32–36.
- (37) Zhao, Q. R.; Gao, Y.; Bai, X.; Wu, C. Z.; Xie, Y. *Eur. J. Inorg. Chem.* **2006**, 1643–1648.
- (38) Zhang, D. F.; Sun, L. D.; Yin, J. L.; Yan, C. H. *Adv. Mater.* **2003**, *15*, 1022–1025.
- (39) Wang, Y.; Zeng, H. C.; Lee, J. Y. *Adv. Mater.* **2006**, *18*, 645–649.
- (40) Ariga, K.; Ji, Q.; McShane, M. J.; Lvov, Y. M.; Vinu, A.; Hill, J. P. *Chem. Mater.* **2011**, *24*, 728–737.
- (41) Wu, H. B.; Chen, J. S.; Lou, X. W.; Hng, H. H. *J. Phys. Chem. C* **2011**, *115*, 24605–24610.
- (42) Su, B.-L.; Sanchez, C.; Yang, X.-Y. *Insights into Hierarchically Structured Porous Materials: From Nanoscience to Catalysis, Separation, Optics, Energy, and Life Science*; Wiley-VCH: Weinheim, Germany, 2011; pp 1–27.
- (43) Tang, Z.; Kotov, N. A. *Adv. Mater.* **2005**, *17*, 951–962.
- (44) Gong, J.; Li, G.; Tang, Z. *Nano Today* **2012**, *7*, 564–585.
- (45) Gao, Y.; Tang, Z. *Small* **2011**, *7*, 2133–2146.
- (46) Dou, X.; Sabba, D.; Mathews, N.; Wong, L. H.; Lam, Y. M.; Mhaisalkar, S. *Chem. Mater.* **2011**, *23*, 3938–3945.
- (47) Li, Z.; Zhou, Y.; Yu, T.; Liu, J.; Zou, Z. *CrystEngComm* **2012**, *14*, 6462–6468.
- (48) Sun, P.; You, L.; Sun, Y.; Chen, N.; Li, X.; Sun, H.; Ma, J.; Lu, G. *CrystEngComm* **2012**, *14*, 1701–1708.
- (49) Kumar, V.; Govind, A.; Nagarajan, R. *Inorg. Chem.* **2011**, *50*, 5637–5645.
- (50) Wu, S.; Yuan, S.; Shi, L.; Zhao, Y.; Fang, J. *J. Colloid Interface Sci.* **2010**, *346*, 12–16.
- (51) Choi, J. K.; Hwang, I. S.; Kim, S. J.; Park, J. S.; Park, S. S.; Jeong, U.; Kang, Y. C.; Lee, J. H. *Sens. Actuators, B* **2010**, *150*, 191–199.
- (52) Shi, W. D.; Song, S. Y.; Zhang, H. J. *Chem. Soc. Rev.* **2013**, *42*, 5714–5743.
- (53) Hossain, M. A.; Yang, G.; Parameswaran, M.; Jennings, J. R.; Wang, Q. *J. Phys. Chem. C* **2010**, *114*, 21878–21884.
- (54) Kang, S. H.; Choi, S. H.; Kang, M. S.; Kim, J. Y.; Kim, H. S.; Hyeon, T.; Sung, Y. E. *Adv. Mater.* **2008**, *20*.
- (55) Roy, P.; Berger, S.; Schmuki, P. *Angew. Chem., Int. Ed.* **2011**, *50*, 2904–2939.
- (56) Liu, B.; Aydil, E. S. *J. Am. Chem. Soc.* **2009**, *131*, 3985–3990.
- (57) Ariga, H.; Taniike, T.; Morikawa, H.; Tada, M.; Min, B. K.; Watanabe, K.; Matsumoto, Y.; Ikeda, S.; Saiki, K.; Iwasawa, Y. *J. Am. Chem. Soc.* **2009**, *131*, 14670–14672.
- (58) Han, X.; Kuang, Q.; Jin, M.; Xie, Z.; Zheng, L. *J. Am. Chem. Soc.* **2009**, *131*, 3152–3153.
- (59) Carpenter, M. K.; Moylan, T. E.; Kukreja, R. S.; Atwan, M. H.; Tessema, M. M. *J. Am. Chem. Soc.* **2012**, *134*, 8535–8542.
- (60) Liu, S.; Yu, J.; Jaroniec, M. *Chem. Mater.* **2011**, *23*, 4085–4093.
- (61) Hengerer, R.; Kavan, L.; Krtil, P.; Grätzel, M. *J. Electrochem. Soc.* **2000**, 147.
- (62) Lin, Y. S.; Duh, J. G.; Hung, M. H. *J. Phys. Chem. C* **2010**, *114*, 13136–13141.
- (63) Lou, X. W.; Chen, J. S.; Chen, P.; Archer, L. A. *Chem. Mater.* **2009**, *21*, 2868–2874.
- (64) Lou, X. W.; Wang, Y.; Yuan, C. L.; Lee, J. Y.; Archer, L. A. *Adv. Mater.* **2006**, *18*, 2325–2329.
- (65) Zhang, H.; Hu, C.; Chen, S.; Zhang, K.; Wang, X. *Catal. Lett.* **2012**, *142*, 809–815.
- (66) Sun, P.; Yu, Y.; Xu, J.; Sun, Y.; Ma, J.; Lu, G. *Sens. Actuators, B* **2011**, *160*, 244–250.
- (67) Cheng, G.; Wang, J. M.; Liu, X. W.; Huang, K. X. *J. Phys. Chem. B* **2006**, *110*, 16208–16211.
- (68) Wang, H. Z.; Liang, J. B.; Fan, H.; Xi, B. J.; Zhang, M. F.; Xiong, S. L.; Zhu, Y. C.; Qian, Y. T. *J. Solid State Chem.* **2008**, *181*, 122–129.
- (69) Liu, S. Q.; Li, Y. X.; Xie, M. J.; Guo, X. F.; Ji, W. J.; Ding, W. P.; Chen, Y. *Nanosci. Nanotechnol.* **2010**, *10*, 6725–6731.
- (70) Yang, R.; Gu, Y. G.; Li, Y. Q.; Zheng, J.; Li, X. G. *Acta Mater.* **2010**, *58*, 866–874.
- (71) Wang, Q.; Zhang, L.-S.; Wu, J.-F.; Wang, W. D.; Song, W.-G.; Wang, W. *J. Phys. Chem. C* **2010**, *114*, 22671–22676.
- (72) Sun, P.; Zhao, W.; Cao, Y.; Guan, Y.; Sun, Y.; Lu, G. *CrystEngComm* **2011**, *13*, 3718–3724.
- (73) Yin, X. M.; Li, C. C.; Zhang, M.; Hao, Q. Y.; Liu, S.; Chen, L. B.; Wang, T. H. *J. Phys. Chem. C* **2010**, *114*, 8084–8088.
- (74) Kim, H.-R.; Choi, K.-I.; Lee, J.-H.; Akbar, S. A. *Sens. Actuators, B* **2009**, *136*, 138–143.
- (75) Wang, H.; Dou, K.; Teoh, W. Y.; Zhan, Y.; Hung, T. F.; Zhang, F.; Xu, J.; Zhang, R.; Rogach, A. L. *Adv. Funct. Mater.* **2013**, DOI: 10.1002/adfm.201300303.
- (76) Cheng, B.; Russell, J. M.; Shi, Zhang, L.; Samulski, E. T. *J. Am. Chem. Soc.* **2004**, *126*, 5972–5973.
- (77) Birkel, A.; Loges, N.; Mugnaioli, E.; Branscheid, R.; Koll, D.; Frank, S.; Panthofer, M.; Tremel, W. *Langmuir* **2010**, *26*, 3590–3595.
- (78) Wang, H.; Wang, Y.; Xu, J.; Yang, H.; Lee, C.-S.; Rogach, A. L. *Langmuir* **2012**, *28*, 10597–10601.
- (79) Guo, Y. Q.; Tan, R. Q.; Li, Y.; Song, W. J. *Appl. Surf. Sci.* **2012**, *258*, 1958–1963.
- (80) Liu, G.; Yu, J. C.; Lu, G. Q.; Cheng, H.-M. *Chem. Commun.* **2011**, *47*, 6763–6783.
- (81) Tian, N.; Zhou, Z.-Y.; Sun, S.-G.; Ding, Y.; Wang, Z. L. *Science* **2007**, *316*, 732–735.
- (82) Chen, J. S.; Luan, D. Y.; Li, C. M.; Boey, F. Y. C.; Qiao, S. Z.; Lou, X. W. *Chem. Commun.* **2010**, *46*, 8252–8254.
- (83) Zhang, H. M.; Han, Y. H.; Liu, X. L.; Liu, P. R.; Yu, H.; Zhang, S. Q.; Yao, X. D.; Zhao, H. J. *Chem. Commun.* **2010**, *46*, 8395–8397.
- (84) Xiang, Q.; Yu, J.; Jaroniec, M. *Chem. Commun.* **2011**, *47*, 4532–4534.
- (85) Wang, J.; Tafen, D. N.; Lewis, J. P.; Hong, Z.; Manivannan, A.; Zhi, M.; Li, M.; Wu, N. *J. Am. Chem. Soc.* **2009**, *131*, 12290–12297.
- (86) Zuo, F.; Wang, L.; Wu, T.; Zhang, Z.; Borchardt, D.; Feng, P. *J. Am. Chem. Soc.* **2010**, *132*, 11856–11857.
- (87) Liu, G.; Yang, H. G.; Wang, X. W.; Cheng, L. N.; Pan, J.; Lu, G. Q.; Cheng, H. M. *J. Am. Chem. Soc.* **2009**, *131*, 12868–12869.

- (88) Liu, M.; Piao, L. Y.; Lu, W. M.; Ju, S. T.; Zhao, L.; Zhou, C. L.; Li, H. L.; Wang, W. J. *Nanoscale* **2010**, *2*, 1115–1117.
- (89) Yang, X. H.; Li, Z.; Sun, C.; Yang, H. G.; Li, C. *Chem. Mater.* **2011**, *23*, 3486–3494.
- (90) Kresse, G.; Furthmüller, J. *Phys. Rev. B* **1996**, *54*, 11169–11186.
- (91) Kresse, G.; Hafner, J. *Phys. Rev. B* **1993**, *48*, 13115–13118.
- (92) Jiang, L. Y.; Wu, X. L.; Guo, Y. G.; Wan, L. J. *J. Phys. Chem. C* **2009**, *113*, 14213–14219.
- (93) Wang, W.; Dahl, M.; Yin, Y. *Chem. Mater.* **2012**, *25*, 1179–1189.
- (94) Yang, H. G.; Zeng, H. C. *J. Phys. Chem. B* **2004**, *108*, 3492–3495.
- (95) Sun, Y.; Wiley, B.; Li, Z.-Y.; Xia, Y. *J. Am. Chem. Soc.* **2004**, *126*, 9399–9406.
- (96) Du, N.; Zhang, H.; Chen, J.; Sun, J. Y.; Chen, B. D.; Yang, D. R. *J. Phys. Chem. B* **2008**, *112*, 14836–14842.
- (97) Yang, H. X.; Qian, J. F.; Chen, Z. X.; Ai, X. P.; Cao, Y. L. *J. Phys. Chem. C* **2007**, *111*, 14067–14071.
- (98) Ding, S.; Lou, X. *Nanoscale* **2011**, *3*, 3586–3588.
- (99) Yan, W. W.; Fang, M.; Tan, X. L.; Liu, M.; Liu, P. S.; Hu, X. Y.; Zhang, L. D. *Mater. Lett.* **2010**, *64*, 2033–2035.
- (100) Zeng, H. C. *J. Mater. Chem.* **2006**, *16*, 649–662.
- (101) Zeng, H. C. *J. Mater. Chem.* **2011**, *21*, 7511–7526.
- (102) Shi, L.; Bao, K. Y.; Cao, J.; Qian, Y. T. *Appl. Phys. Lett.* **2008**, *93*, 152511.
- (103) Wang, H.; Fu, F.; Zhang, F.; Wang, H.-E.; Kershaw, S. V.; Xu, J.; Sun, S.-G.; Rogach, A. L. *J. Mater. Chem.* **2012**, *22*, 2140–2148.
- (104) Wang, Y. F.; Lei, B. X.; Hou, Y. F.; Zhao, W. X.; Liang, C. L.; Su, C. Y.; Kuang, D. B. *Inorg. Chem.* **2010**, *49*, 1679–1686.
- (105) Law, M.; Greene, L. E.; Johnson, J. C.; Saykally, R.; Yang, P. *Nat. Mater.* **2005**, *4*, 455–459.
- (106) Vayssieres, L.; Graetzel, M. *Angew. Chem., Int. Ed.* **2004**, *43*, 3666–3670.
- (107) So, S.; Lee, K.; Schmuki, P. *J. Am. Chem. Soc.* **2012**, *134*, 11316–11318.
- (108) Roy, P.; Das, C.; Lee, K.; Hahn, R.; Ruff, T.; Moll, M.; Schmuki, P. *J. Am. Chem. Soc.* **2011**, *133*, 5629–5631.
- (109) Kolmakov, A.; Zhang, Y.; Cheng, G.; Moskovits, M. *Adv. Mater.* **2003**, *15*, 997–1000.
- (110) Zheng, M.; Li, G.; Zhang, X.; Huang, S.; Lei, Y.; Zhang, L. *Chem. Mater.* **2001**, *13*, 3859–3861.
- (111) Krishnamoorthy, T.; Tang, M. Z.; Verma, A.; Nair, A. S.; Pliszka, D.; Mhaisalkar, S. G.; Ramakrishna, S. *J. Mater. Chem.* **2012**, *22*, 2166–2172.
- (112) Wang, J.; Du, N.; Zhang, H.; Yu, J.; Yang, D. *J. Phys. Chem. C* **2011**, *115*, 11302–11305.
- (113) Shinde, D. V.; Lim, I.; Kim, C. S.; Lee, J. K.; Mane, R. S.; Han, S.-H. *Chem. Phys. Lett.* **2012**, *542*, 66–69.
- (114) Wang, D.; Yang, J.; Li, X.; Wang, J.; Li, R.; Cai, M.; Sham, T. K.; Sun, X. *Cryst. Growth Des.* **2011**, *12*, 397–402.
- (115) Ghosh, S.; Das, K.; Chakrabarti, K.; De, S. K. *CrystEngComm* **2012**, *14*, 929–935.
- (116) Shinde, D. V.; Mane, R. S.; Oh, I. H.; Lee, J. K.; Han, S. H. *Dalton Trans.* **2012**, *41*, 10161–10163.
- (117) Kuang, Q.; Xu, T.; Xie, Z.-X.; Lin, S.-C.; Huang, R.-B.; Zheng, L.-S. *J. Mater. Chem.* **2009**, *19*, 1019–1023.
- (118) Lei, D.; Zhang, M.; Hao, Q.; Chen, L.; Li, Q.; Zhang, E.; Wang, T. *Mater. Lett.* **2011**, *65*, 1154–1156.
- (119) Pan, S. S.; Shen, Y. D.; Teng, X. M.; Zhang, Y. X.; Li, L.; Chu, Z. Q.; Zhang, J. P.; Li, G. H.; Hu, X. *Mater. Res. Bull.* **2009**, *44*, 2092–2098.
- (120) Huang, H.; Lim, C. K.; Tse, M. S.; Guo, J.; Tan, O. K. *Nanoscale* **2012**, *4*, 1491–1496.
- (121) Shi, L.; Xu, Y.; Li, Q. *Nanoscale* **2010**, *2*, 2104–2108.
- (122) Wang, H.; Yang, H.; He, L.; Kalytchuk, S.; Hu, C.; Teoh, W. Y.; Rogach, A. L., 2013, in preparation.
- (123) Chen, H.-Y.; Kuang, D.-B.; Su, C.-Y. *J. Mater. Chem.* **2012**, *22*, 15475–15489.
- (124) Drake, C.; Seal, S. *Appl. Phys. Lett.* **2007**, *90*, 233117.
- (125) Chao, J.; Xu, X.; Huang, H.; Liu, Z.; Liang, B.; Wang, X.; Ran, S.; Chen, D.; Shen, G. *CrystEngComm* **2012**, *14*, 6654–6658.
- (126) Liu, X. M.; Wu, S. L.; Chu, P. K.; Zheng, J.; Li, S. L. *Mater. Sci. Eng., A* **2006**, *426*, 274–277.
- (127) Wang, H.; Xi, L.; Tucek, J.; Zhan, Y.; Hung, T. F.; Kershaw, S. V.; Zboril, R.; Chung, C. Y.; Rogach, A. L. *Nanoscale* **2013**, DOI: 10.1039/C3NR02456C.
- (128) Han, S. J.; Jang, B. C.; Kim, T.; Oh, S. M.; Hyeon, T. *Adv. Funct. Mater.* **2005**, *15*, 1845–1850.
- (129) Liu, J.; Li, W.; Manthiram, A. *Chem. Commun.* **2010**, *46*, 1437–1439.
- (130) Xu, C.; Sun, J.; Gao, L. *J. Mater. Chem.* **2012**, 975–979.
- (131) Jin, Y.-H.; Min, K.-M.; Seo, S.-D.; Shim, H.-W.; Kim, D.-W. *J. Phys. Chem. C* **2011**, *115*, 22062–22067.
- (132) Zhai, C.; Du, N.; Zhang, H.; Yu, J.; Yang, D. *ACS Appl. Mater. Interfaces* **2011**, *3*, 4067–4074.
- (133) Tarascon, J. M.; Armand, M. *Nature* **2001**, *414*, 359–367.
- (134) Li, Y.; Zhu, S.; Liu, Q.; Gu, J.; Guo, Z.; Chen, Z.; Feng, C.; Zhang, D.; Moon, W.-J. *J. Mater. Chem.* **2012**, 2766–2773.
- (135) Wu, P.; Du, N.; Zhang, H.; Yu, J.; Yang, D. *J. Phys. Chem. C* **2010**, *114*, 22535–22538.
- (136) Xin, X.; Zhou, X.; Wu, J.; Yao, X.; Liu, Z. *ACS Nano* **2012**, *6*, 11035–11043.
- (137) Myung, S.-T.; Takahashi, N.; Komaba, S.; Yoon, C. S.; Sun, Y.-K.; Amine, K.; Yashiro, H. *Adv. Funct. Mater.* **2011**, *21*, 3231–3241.
- (138) Lee, J. H. *Sens. Actuators, B* **2009**, *140*, 319–336.
- (139) Srivastava, V.; Jain, K. *Sens. Actuators, B* **2008**, *133*, 46–52.
- (140) Pang, H.; Yang, H.; Guo, C. X.; Li, C. M. *ACS Appl. Mater. Interfaces* **2012**, *4*, 6261–6265.
- (141) Kim, Y. J.; Kim, K. H.; Kang, P.; Kim, H. J.; Choi, Y. S.; Lee, W. I. *Langmuir* **2012**, *28*, 10620–10626.
- (142) Liu, M.; Yang, J.; Feng, S.; Zhu, H.; Zhang, J.; Li, G.; Peng, J. *Mater. Lett.* **2012**, *76*, 215–218.
- (143) Ferrere, S.; Zaban, A.; Gregg, B. A. *J. Phys. Chem. B* **1997**, *101*, 4490–4493.
- (144) Docampo, P.; Tiwana, P.; Sakai, N.; Miura, H.; Herz, L.; Murakami, T.; Snaith, H. J. *J. Phys. Chem. C* **2012**, *116*, 22840–22846.